

Online Guided Wave-Based Debonding Detection in Honeycomb Sandwich Structures

F. Song* and G. L. Huang†

University of Arkansas at Little Rock, Little Rock, Arkansas 72204

and

G. K. Hu‡

Beijing Institute of Technology, 100081 Beijing, People's Republic of China

DOI: 10.2514/1.J050891

Because of the complex nature of structural characteristics, damage detection in honeycomb sandwich structures inherently carries many challenges. In the study, effects of debonding on leaky guided wave propagation in honeycomb sandwich structures are first studied by using the finite element method. A surface-bonded piezoelectric wafer actuator/sensor network is used for elastic-guided wave propagation and reception in the composite. Experimental testing is then conducted to verify the numerical simulation and for damage detection. A damage localization image from each actuator-sensor pair is constructed by conducting probability analysis of differential features of transmitted guided waves in the structure with and without debonding. An image of the whole structure is then reconstructed by superimposing the image from each actuator-sensor pair. The quality of the final image is improved by using the image fusion technique. To detect multiple debondings in the honeycomb sandwich structure, a multilevel sensor network strategy is suggested for eliminating pseudoimages due to image coupling of multiple debondings. The final structure image demonstrates that the proposed method can provide quantitative information about location and size of debonding in the honeycomb sandwich structure.

Nomenclature

F^b	=	filtered guided wave signals from specimens without debonding in the frequency domain
F^d	=	filtered guided wave signals from specimens with debonding in the frequency domain
f	=	frequency
f_c	=	central frequency
f_1	=	low cutoff frequency of the guided wave signal
f_2	=	high cutoff frequency of the guided wave signal
$H(t)$	=	Heaviside step function
l_{ij}	=	distance between the actuator # i and sensor # j
P_d	=	damage localization probability of arbitrary position (x, y) within the sensor network
P_{ij}	=	damage distribution probability estimated from the actuator-sensor pair (# $i, #j$)
SDC_{ij}	=	signal difference coefficient from the actuator-sensor pair (# $i, #j$)
t	=	time
V	=	amplitude of the excitation signal
α	=	scaling parameter
ω_1	=	lower limit of the narrowband excitation frequency
ω_2	=	upper limit of the narrowband excitation frequency

I. Introduction

DUE to attractive characteristics such as high strength/stiffness-to-weight ratios and effective acoustic insulation, honeycomb sandwich structures have been used extensively in marine,

aerospace, and aeronautic industries [1,2]. However, an intensive load or repeating loading in the core tends to induce debonding along the skin-core interface, threatening the integrity and safety of the whole structure [3]. Conventional evaluation approaches such as C-scan and X-ray are limited to a time-consuming, point-by-point methodology and require bulky instruments, which makes them unsuitable to be directly applied to online monitor aircraft structures. Therefore, development of an active online monitoring system for composite structures becomes an urgent issue and has received considerable attention recently [4–8]. Compared with conventional nondestructive evaluation (NDE) techniques, online structural health monitoring (SHM) techniques can instantaneously provide reliable and quantitative structural health information for in-service structures and cover a relatively large inspection area [9,10].

Ultrasonic guided wave (GW)-based SHM technique has shown great potential for delamination detection in laminated composites [11–13]. By using piezoelectric actuators/sensors, Su and his collaborators [14,15] used the time of flight (TOF) between the incipient fundamental symmetric Lamb wave and the delamination-induced fundamental shear horizontal mode to triangulate delaminations in composite laminates. Wang and Yuan [16] performed prestack reverse-time migration technique to image the delaminations in composite laminates with a linear piezoelectric lead zirconate titanate (PZT) disk array, and both the location and size of the delaminations were quantitatively obtained. Based on selective Lamb wave transducers, Petculescu et al. [17] demonstrated that accumulated time delay of the group velocity is a reliable damage parameter for quantitative monitoring of delaminations for quasi-isotropic woven and cross-ply composites. However, those approaches are limited to significant scattered waves or obvious wave velocity change caused by damages as primary damage characteristics, which may not be observed in some engineering structures.

Owing to the dramatic acoustic impedance difference between the core and skin as well as high core-to-skin thickness ratio, wave propagation in honeycomb sandwich structures can be characterized as leaky GWs when wave frequency is sufficiently high [18,19]. The mechanism of the GW energy being dissipated into the core results in significant wave attenuation. From a through-transmission test using angle beam transducers, a GW mode sensitive to skin-core debonding, at a given phase velocity and frequency, was found by

Received 30 August 2010; revision received 24 June 2011; accepted for publication 27 August 2011. Copyright © 2011 by the American Institute of Aeronautics and Astronautics, Inc. All rights reserved. Copies of this paper may be made for personal or internal use, on condition that the copier pay the \$10.00 per-copy fee to the Copyright Clearance Center, Inc., 222 Rosewood Drive, Danvers, MA 01923; include the code 0001-1452/12 and \$10.00 in correspondence with the CCC.

*Ph.D. Candidate, Department of Systems Engineering, 2801 South University Avenue. Student Member AIAA.

†Associate Professor, Department of Systems Engineering, 2801 South University Avenue; glhuang@ualr.edu.

‡Professor, School of Aerospace Engineering, 5 South Zhongguancun Street.

comparing wave propagation through a perfectly bonded area and a debonded area under the same testing condition. Neither scattered waves nor wave velocity changes due to skin-core debonding were obviously found experimentally [20]. However, a significant increase in the received signal amplitude was observed when the GW propagates through the debonded area in honeycomb sandwich structures [20,21].

To identify skin-core delamination or debonding in honeycomb sandwich structures, interpretation of leaky GWs has been regarded as a promising approach because significant changes in amplitudes of the transmitted GW signals can be observed in both time and frequency domains. Hay et al. [20] theoretically simulated leaky Lamb waves in the composite skin. The sensitivities of various Lamb wave modes to the composite skin-Nomex core debonding were studied through frequency sweeping. Using the leaky surface wave propagation in the honeycomb composite, Qi et al. [22] compared ultrasonic wave transmission energy between the specimen at normal conditions and the debonding specimen to identify the skin-core debonding. However, a quantitative assessment of debonding information was not provided. Based on the damage index approach, Baid et al. [23] identified and located composite skin-honeycomb core debonding using ultrasonic sensor arrays. In the work, clusters of sensor arrangements were required to precisely locate the skin-core debonding, and information about the damage size was completely left unknown. Recently, efforts have been made to develop effective diagnostic imaging strategies, and the probability analysis-based algorithm has been proposed to image cracks and corrosion in composite laminates and aircraft wings [24,25]. There is a lack of an efficient and systematic debonding detection technique for honeycomb sandwich structures by using a sparse actuator/sensor network, especially for the multidebonding detection. It was reported that appearance of multidamage usually leads to much more intricate wave phenomena, and thus predictions for multidamage could be highly uncertain or ambiguous [26,27].

In this paper, a three-dimensional finite element model, which takes into account the real geometry of regular hexagonal honeycomb core, is first used to simulate debonding influences on the leaky GW propagation. In the numerical simulation, a commercially available finite element (FE) code ANSYS/Multiphysics is used to simulate wave propagation and wave reception by the surface-bonded piezoelectric actuators/sensors. The coupled electro-mechanical behavior is considered by directly applying electric voltages. An experimental study is then conducted to verify the numerical simulation and for damage detection. An appropriate signal difference coefficient is defined to represent the differential features of debonding. To minimize noise effects, the measurement signals are filtered out by using a Fourier transform filter method. A damage localization image at each frequency is formed by conducting probability analysis of differential features of transmitted guided waves in the structure with and without debonding for each actuator-sensor pair. An imaging area is then reconstructed by superimposing the image from each actuator-sensor path. The final image of the whole structure can subsequently be obtained by fusing images from multiple frequencies. To detect multiple debondings in the honeycomb sandwich structure, a multilevel sensor network strategy is proposed. The final image results demonstrate that the proposed approach can provide reliable quantitative information about location and size of debonding in the honeycomb sandwich structure.

II. Numerical Simulation of the Leaky GWs

Because of complex structural geometry and boundary conditions, it is not practical, and may be impossible, to analytically predict the GW propagation in honeycomb sandwich structures. In this section, the leaky GW propagation generated by a surface-bonded PZT actuator/sensor system is investigated based on the three-dimensional finite element (FE) model. Specific attention will be paid to debonding effects on the leaky GW propagation. A commercially available finite element code, ANSYS/Multiphysics 11.0, is used. In the FE modeling, the SOLID5 element with eight nodes

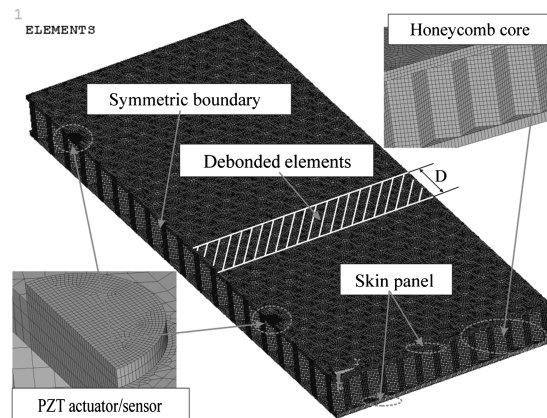


Fig. 1 The FE model of a debonded honeycomb sandwich structure with the surface-bonded PZT patches.

and six degrees of freedoms (DOF) at each node is selected for the PZT patches to consider electromechanical coupling behavior. The additional DOF in the coupled field element is electrical voltage. Input voltage can be applied on the top nodes of the PZT actuator, and zero voltage is assigned on the bottom nodes of the PZT actuator and sensor for the simulation of grounding operation. The SOLID45 element is used to model two skin panels, and the SHELL63 element is considered to model real geometry of the hexagonal cells. The debonding is simulated by releasing the coupling condition of the nodes along the interface between the skin panel and the honeycomb core in the debonded area. The FE model of a honeycomb sandwich structure with a through debonding along the width direction between two surface-bonded PZT patches is shown in Fig. 1. In the simulation, the debonding with length D is assumed to be 55.32 mm away from the PZT actuator, and the actuator-sensor distance is 172.8 mm. The geometry parameters of the composite are shown in Table 1.

Because of the symmetry of the problem, only a half-volume of the structure is taken into consideration, and a symmetric boundary condition is applied (see Fig. 1). For the convergence of dynamic simulation, mesh of the structure should be fine enough such that at least 10 elements exist per wavelength along the direction of wave propagation. The integration time step should also be sufficiently small to resolve the frequency response of the structure.

The aluminum alloy T6061 and Nomex are used for skin panel and core material in the simulation, respectively. The material properties are shown in Table 2.

The piezoelectric material properties are assumed as

$$[\varepsilon] = \begin{bmatrix} 6.45 & 0 & 0 \\ & 6.45 & 0 \\ & \text{Symmetry} & 5.62 \end{bmatrix} \times 10^{-9} \text{ CV}^{-1} \cdot \text{m}^{-1}$$

$$[e] = \begin{bmatrix} 0 & 0 & -5.2 \\ 0 & 0 & -5.2 \\ 0 & 0 & 15.1 \\ 0 & 0 & 0 \\ 0 & 12.7 & 0 \\ 12.7 & 0 & 0 \end{bmatrix} \text{ C} \cdot \text{m}^{-2}$$

and

$$[c] = \begin{bmatrix} 13.9 & 6.78 & 7.43 & 0 & 0 & 0 \\ & 13.9 & 7.43 & 0 & 0 & 0 \\ & & 11.5 & 0 & 0 & 0 \\ & & & 3.56 & 0 & 0 \\ & & & & 2.56 & 0 \\ & & \text{Symmetry} & & & 2.56 \end{bmatrix} \times 10^{10} \text{ Pa}$$

Table 1 Geometry parameters of the honeycomb sandwich structure and PZT actuator/sensor

Skin panels				Honeycomb core		PZT actuator-sensor	
Length, mm	Width, mm	Thickness, mm	Cell size, mm	Wall thickness, mm	Height, mm	Diameter, mm	Thickness, mm
268.8	99.8	2.0	4.8	0.22	15.0	6.35	0.76

Table 2 Material properties of skins and honeycomb core

Material	Young's modulus, GPa	Poisson's ratio	Density, $\text{kg} \cdot \text{m}^{-3}$
Aluminum alloy T6061	70	0.33	2700
Nomex	9	0.30	1384

where $[e]$ is the dielectric matrix, $[e]$ is the piezoelectric matrix, and $[c]$ is the stiffness matrix. The density of the PZT material is assumed to be $7700 \text{ kg} \cdot \text{m}^{-3}$.

To reduce dispersive effects on the GW propagation, the excitation signal concentrated in a small range around the central frequency is used, which is beneficial for the interpretation of the received data. A five-peak narrow band tone burst signal is selected as

$$V_{in}(t) = V \left[H(t) - H\left(t - \frac{5}{f_c}\right) \right] \left[1 - \cos\left(\frac{2\pi f_c t}{5}\right) \right] \sin(2\pi f_c t) \quad (1)$$

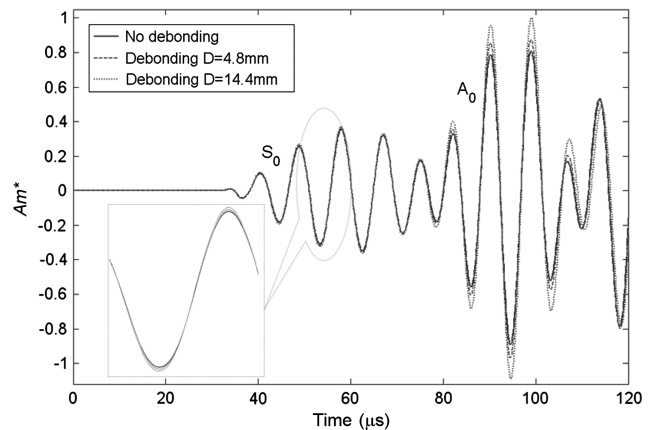
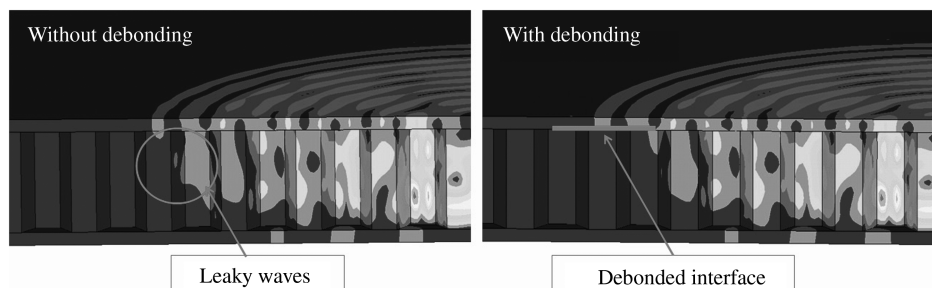
where V is the amplitude of the excitation signal, f_c is the central frequency, t is time, and $H(t)$ is the Heaviside step function.

The GW propagation in perfectly bonded honeycomb sandwich structures has been investigated for a wide range of frequencies based on the FE simulation [19]. To study debonding effects on the GW propagation, FE simulation of the GW propagation is conducted in the honeycomb sandwich structures without and with debonding. Both models have the same geometry and loading condition. Figure 2 shows the snapshots of the wave field magnitude at time $t = 42 \mu\text{s}$, when the GWs just reach the areas without and with debonding. The excitation frequency in the figure is $f_c = 110 \text{ kHz}$ and the debonding size is $D = 14.4 \text{ mm}$, and the minimum wavelength of the GW modes can be estimated to be around 12 mm based on the dispersion curve of the upper plate. Based on the wave fields in Fig. 2, it can be found that the GWs exhibit leaky properties in the range of the perfectly bonded area; however, there is no leakage of the GWs into the core in the debonded area. Therefore, the leaky GWs can propagate a relatively longer distance with less decay in the debonded structure than in the perfectly bonded structure. The numerical simulation also reveals that there is no leaky energy in the debonded area for other higher-excitation frequencies.

The debonding size influences on the GW propagation are then considered by quantitatively examining the sensor responses. Figure 3 shows comparison of the normalized sensor signals in the honeycomb sandwich structures without and with debonding at frequency $f_c = 110 \text{ kHz}$. Lengths of the through debonding are $D = 4.8 \text{ mm}$ and $D = 14.4 \text{ mm}$, respectively. In the figure, $Am^* = Am/Am_{\max}$ is the normalized sensor amplitude with Am being the

magnitude of the sensor voltage signal and Am_{\max} being the maximum value of all plotted sensor magnitudes. From Fig. 3, it can be observed that both the lowest symmetric mode S_0 and the lowest antisymmetric mode A_0 are favorably generated at current frequency based on the group velocity analysis, and the amplitudes of the GWs are changed due to the presence of the debonding. The sensor signals after $110 \mu\text{s}$ are boundary reflected waves that can be avoided by enlarging the dimension of the structural model, but significant computational time will be increased. The signal amplitude increases with the increase of the size of the debonding for both A_0 and S_0 modes, as indicated in Fig. 3. This is attributed to the fact that less wave energy dissipates into the core when the GWs propagate through the debonded area. It is also noticed that the phase velocity of the GW modes has not been changed due to the appearance of the debonding. Specifically, the A_0 mode is more sensitive to the debonding than the S_0 mode, which can be readily understood by analyzing the ratio of in-plane and out-of-plane displacements at the interface for a given wave mode [19].

To clearly illustrate the wave mode sensitivity, the normalized theoretical wave structures along the thickness of the upper plate are then plotted in Fig. 4 at frequency $f = 110 \text{ kHz}$ for the S_0 mode and the A_0 mode, respectively. It can be observed that the in-plane displacement is dominated for the S_0 mode, whereas the out-of-plane displacement is much larger than the in-plane displacement for the A_0 mode. As a result, it can be expected that most wave energy is retained in the upper plate for the S_0 mode; however, more wave energy of the A_0 mode can be dissipated into the core for the perfectly bonded sandwich structure. Therefore, when the current skin-core

**Fig. 3** FE simulation of the normalized sensor responses in the honeycomb sandwich structure without and with debonding at $f_c = 110 \text{ kHz}$.**Fig. 2** Snapshots of wave-field magnitude at time $t = 42 \mu\text{s}$ and $f_c = 110 \text{ kHz}$ in the FE models of honeycomb sandwich structures without and with debonding.

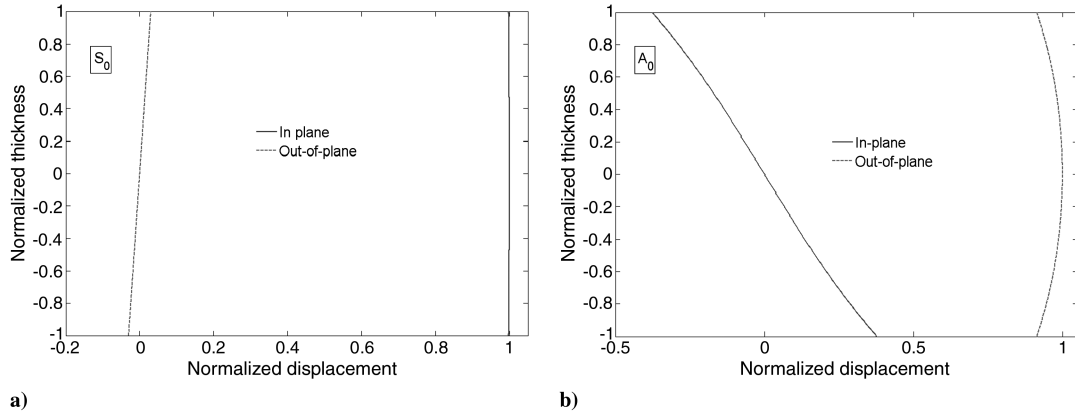


Fig. 4 Theoretical wave structures along the thickness of the plate for $f = 110$ kHz: a) the S_0 mode, and b) the A_0 mode.

structure has a debonding fault, the GW signal of the A_0 mode is more sensitive to inspect the defect.

III. Experimental Study of the Leaky GWs

In the previous section, the debonding influences on the leaky GWs have been studied using the FE simulation. Based on the concept, specific experimental testing with a sparse PZT actuator-sensor network is conducted to generate and receive the leaky GWs in the honeycomb sandwich panels. Application of the leaky GWs for the debonding detection is specifically investigated.

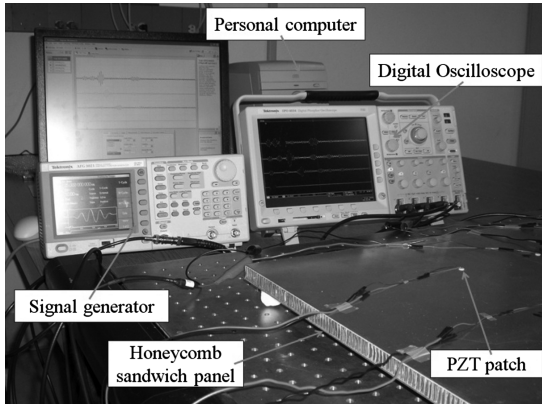


Fig. 5 Testing configuration for an active health monitoring system to detect skin-core debonding in a honeycomb sandwich panel.

A. Experimental Setup

The overall testing configuration is displayed in Fig. 5. The honeycomb sandwich panels, which are composed of aluminum alloy (T6061) skins and hexagonal-celled Nomex core (HRH-78 honeycomb, Hexcel Corporation) with the same material properties as in the FE simulation, are prepared. In the experimental testing, one of the PZT patches can serve as the actuator to generate ultrasonic signals, and the rest function as the sensors to form an “active” local sensing system. The commercial cyanoacrylate adhesive is used to bond the PZT patches to the surface of the specimen. A peak-to-peak value of 10 V of ultrasonic wave signals is generated by the function generator (Tektronix AFG3021) and applied on the PZT actuator to excite the structure. Signals from the sensors are collected by the digital oscilloscope (Tektronix DPO4034) and processed in the personal computer by the software Ni SignalExpress. The transient signals are digitized with 10,000 points using a sampling interval of $0.04 \mu\text{s}$.

Figure 6 shows a layout of a PZT actuator/sensor network bonded on the honeycomb sandwich specimens ($609 \times 609 \times 19$ mm) with interfacial monodebonding N0 (SP #1) and dual-debonding N1 and N2 (SP #2), respectively. Nine PZT patches (6.36 mm in diameter; 0.76 mm in thickness; APC International, Ltd., 850) are used in a square grid pattern with a distance of 126.7 mm between each patch. The interfacial debonding is formed by inserting a rectangular Teflon® film ($30 \times 10 \times 0.1$ mm) into the skin-core interface of the sandwich panels during the process of fabrication. The detailed position of the PZT patches and debonding in the honeycomb sandwich panels can be found in the figure. A honeycomb sandwich panel without any debonding, which has the same geometry and material constants as SP #1 and SP #2, is also tested as a baseline with the same sensor network arrangement in Fig. 6. It should be noted

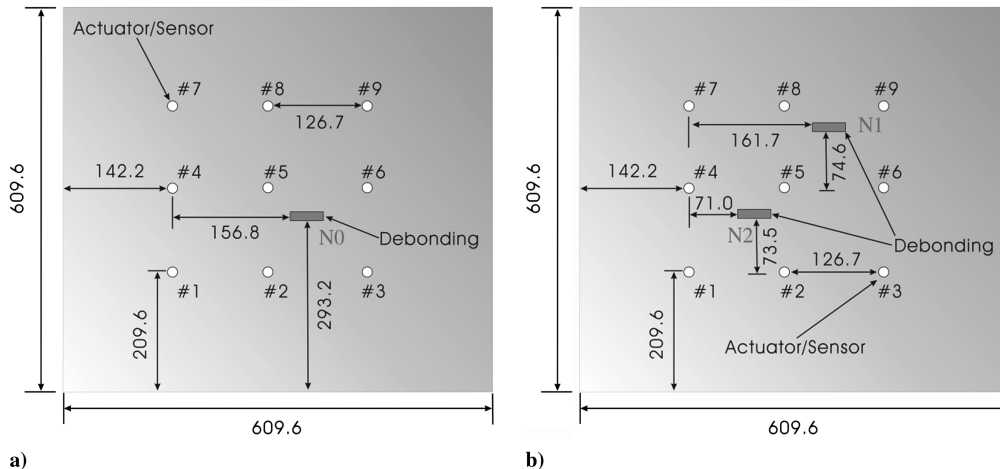


Fig. 6 A layout of the PZT wafers bonded on two honeycomb sandwich specimens: a) monodebonding (SP #1), and b) dual-debonding (SP #2). All measurements in millimeters.

that, for the honeycomb sandwich panels with and without debonding, the variability of commercial PZT patches, manufactured specimens, and bond strength may lead to slight amplitude and velocity changes of sensor signals even for the same experimental configuration. Compensation should be made for the signal variability in the baseline and debonded specimens [28] through the numerical simulation if the signal variability affects the final structure image, which will be discussed in the debonding imaging section. Alternately, a calibrated impact test will be considered in future work to ensure the baseline signal and the debonding signal are collected from exactly the same material configuration.

B. Testing Frequency Selection

Selection of an appropriate driving frequency is crucial for the success of GW-based SHM. For a given platelike structure, it would be ideal to select appropriate wave modes that have the least dispersion and the highest sensitivity to the damage, which can be determined from the structure dispersion curve. Figure 7 shows the experimentally obtained group velocity dispersion curve of the baseline honeycomb sandwich structure [19]. The results indicate that the S_0 mode is not sensitive to the variation of any considered driving frequency. However, the leaky A_0 wave mode is insensitive to small variations in frequency only when the frequency is relatively high, (e.g., $f_c > 150$ kHz), which is suitable for damage detection in the considered honeycomb sandwich structure. In addition, with knowledge of the debonding size (30 mm × 10 mm × 0.1 mm) in the specimen, the driving frequency can be also predicted based on its detection limit and the resolution of the change for the resulted signal. Therefore, balancing these issues, the frequency range 150 to 375 kHz is selected to excite diagnostic GWs for debonding detection in the experimental study where only two fundamental modes exist, which makes the interpretation of the signal easier.

C. Signal Characterization and Processing

The GW data is collected in a through-transmission manner from all possible actuator-sensor combinations based on the current sensor array. The presence of debonding is revealed with the comparison of the received data to the baseline data, where no debonding presents. Figure 8 shows example waveforms collected from the actuator-sensor pair (#3 and #5) on SP #1 at excitation central frequencies $f_c = 175$ kHz and $f_c = 375$ kHz, respectively. For the comparison, the signal from the same actuator-sensor pair without debonding is also included in the figure as the baseline data. It can be found that both the S_0 and A_0 modes are generated at $f_c = 175$ kHz, while only the dominated S_0 mode is clearly seen at $f_c = 375$ kHz. The GW signals are, in a similar manner, obtained for different combinations of actuator-sensor pairs.

From Fig. 8, it can be found that the debonding in the honeycomb sandwich structure mainly results in an observable increase in the amplitude of the sensor signals, which is consistent with the

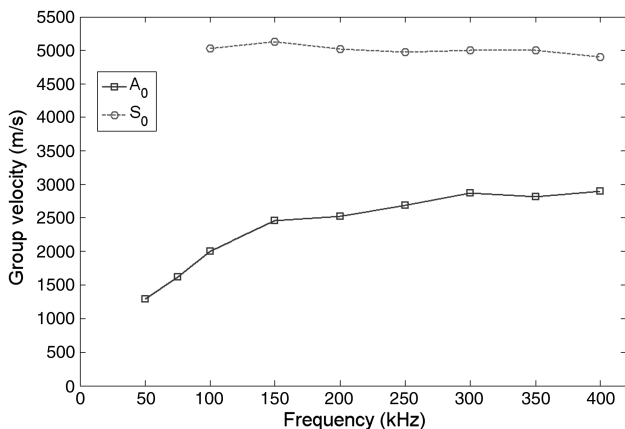


Fig. 7 Group velocity dispersion curve of the honeycomb sandwich structure obtained from the experimental testing.

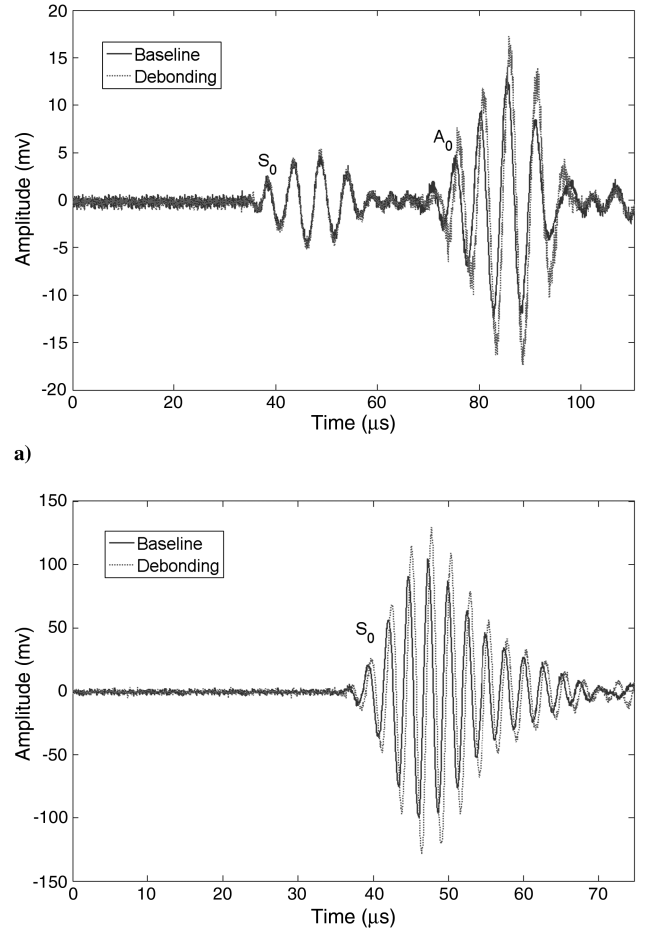


Fig. 8 Received waveforms of the actuator-sensor pair (#3, #5) in the structure with and without debonding at different frequencies: a) $f_c = 175$ kHz, and b) $f_c = 375$ kHz.

prediction from the FE simulation. Comparing with the FE result in Fig. 3, the phase difference between the debonding signal and the baseline signal is observed, which can be attributed to the variability of commercial piezoelectric patches, manufactured specimens, and bond strength in the perfectly bonded and debonded specimens. A number of previous experimental studies used wave scattering or wave attenuation for delamination detection in laminated composites [12,14,15]. However, no scattered waves are clearly observed in the current debonded honeycomb specimen. Therefore, approaches that trace time of flight or group velocity variation [14,17] may not be suitable to capture the debonding characteristics in the honeycomb sandwich structure. In the study, a signal difference coefficient (SDC), the GW feature that accounts for change in signal amplitude, is employed to detect debonding.

To use the SDC values as the feature for debonding detection in the GW method, it is necessary to eliminate or suppress the effects of changes in environmental condition. As shown in Fig. 8, the sensor signal at $f_c = 175$ kHz has relatively low signal-to-noise ratio. To minimize the measurement noise, a Fourier transform (FT)-based filtering is conducted for the sensor signals collected from different actuator-sensor pairs. After taking the FT of the signals, filtered signals then can be reconstructed via the inverse FT by setting integration range to the cutoff frequency band as

$$s(t) = \frac{1}{2\pi} \int_{\omega_1}^{\omega_2} \bar{s}(\omega) e^{-i\omega t} d\omega \quad (2)$$

where ω_1 and ω_2 are the lower and upper limits of the narrowband excitation frequency, respectively. Consequently, frequency components outside the excitation frequencies are filtered out.

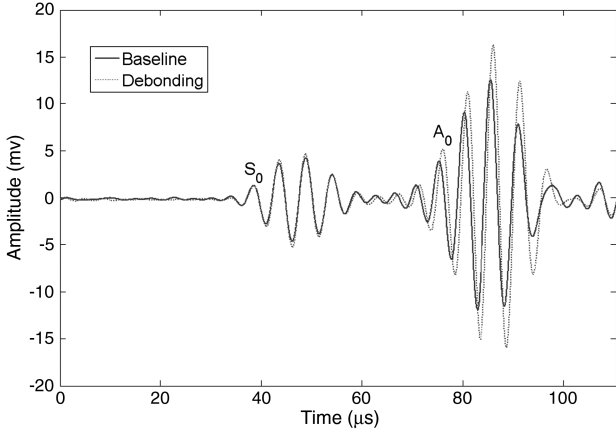


Fig. 9 Filtered signals from sensor signals in Fig. 8a.

Figure 9 displays the filtered sensor signals from the sensor signals in Fig. 8a. It is evident that the background noise can be dramatically reduced, which is useful for further damage characterization.

IV. Debonding Detection by Using Multifrequency GWs

In this section, filtered sensor signals in the experimental testing are used for debonding characterization in honeycomb sandwich structures. The SDC based on the filtered GW signals in the frequency domain is employed to capture the differential features of debonding. To image the debonding, the damage probability distribution is calculated at each pixel by using the extracted SDC as the inputs, and the image at individual frequency is fused to improve the quality of the final image of debonding. A specific inspection strategy using multilevel sensor network is proposed for multidebonding detection.

A. SDC and Debonding Imaging Algorithm

Because of the multimode nature of GWs and the fact that different GW modes interact with different types of structural changes in different ways, there is much flexibility to select the GW feature for damage image reconstruction [29]. The SDC is regarded as an efficient approach to capture the differential features in the transmitted GW signals due to damage. In this subsection, the following SDC is proposed to account for the root-mean-square change of the GW signals from the actuator-sensor pair (#i, #j) as

$$SDC_{ij} = \sqrt{\int_{f_1}^{f_2} [F^d(f) - F^b(f)]^2 df / \int_{f_1}^{f_2} F^b(f)^2 df} \quad (3)$$

in which F^b and F^d are, respectively, filtered GW signals from specimens without and with debonding in the frequency domain; f is

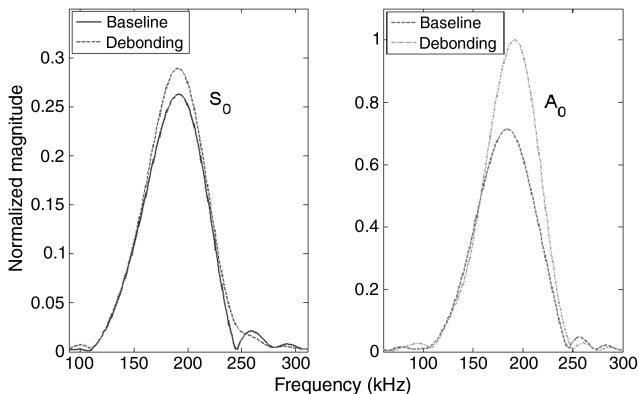


Fig. 10 Frequency spectra of filtered sensor signals from the sensor signals in Fig. 9 for the S_0 and A_0 modes, respectively.

the frequency; and f_1 and f_2 are the cutoff frequency lower and upper bands for the GWs.

Figure 10 shows the frequency spectra of the filtered sensor signals from the measurement data in Fig. 9. A clear difference between the measurement data from the specimens with and without debonding can be found, which indicates great potential for using the SDC as the debonding feature in the honeycomb sandwich structure. The magnitude of the sensor signals increases with the presence of the debonding for both S_0 and A_0 modes. More interestingly, no band dilation can be obviously observed, which shows that the skin-core debonding does not induce severe wave dispersion. The growth of the debonding can be monitored by tracing the magnitude increase in the transmitted GW signals with respect to the baseline. As we expect, the phase difference between the debonding signal and the baseline signal is also reflected in the frequency domain, and there is a slight shift in the driving frequency that gives the peak response for the A_0 mode. However, through the following SDC calculation and the structure image analysis, effects of the phase change on the SDC and structure image are found to be small compared with those of the amplitude change in the signals. In the study, an appropriate damage threshold in the structure image analysis is suggested as compensation for the signal variability and to eliminate effects of the phase difference.

To form the image containing damage information, the inspection area within the sensor network is discretized into a set of image pixels (x, y) , as shown in Fig. 11. Note that the sensor signals from the actuator-sensor pair (#i, #j) should be equal to that from (#i, #j) due to signal reciprocity. Accordingly, for an actuator/sensor network with N discrete PZT patches, $N(N - 1)/2$ sets of data are actually needed. A sequential scan for detecting debonding in the large honeycomb sandwich structure can be performed by alternately exciting one of the transducers while the others work as sensors to measure the transmitted GWs.

The damage localization probability of arbitrary position (x, y) within the sensor network can be expressed as a linear summation of the obtained SDC_{ij} [see Eq. (3)] from every possible actuator-sensor pair, each of which has a spatial distribution as [24,29]

$$P_d(x, y) = \sum_{i=1}^{N-1} \sum_{j=i+1}^N P_{ij}(x, y) = \sum_{i=1}^{N-1} \sum_{j=i+1}^N SDC_{ij} \left[\frac{\alpha - B_{ij}(x, y)}{\alpha - 1} \right] \quad (4)$$

where $P_{ij}(x, y)$ is the damage distribution probability estimated from the actuator-sensor pair (#i, #j); $\frac{\alpha - B_{ij}(x, y)}{\alpha - 1}$ is the spatial distribution function, as illustrated in Fig. 11, which has the contour in the shape of a set of ellipses and is the nonnegative linearly decreasing spatial distribution function of each actuator-sensor pair, and

$$B_{ij}(x, y) = \begin{cases} L_{ij}(x, y), & L_{ij}(x, y) < \alpha \\ \alpha, & L_{ij}(x, y) \geq \alpha \end{cases} \quad (5)$$

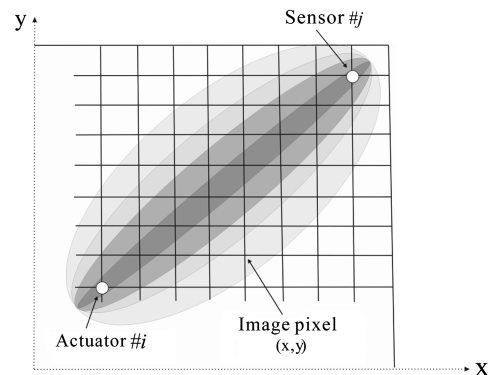


Fig. 11 Illustration of the debonding imaging algorithm with the elliptical distribution function.

and $L_{ij} = [\sqrt{(x-x_i)^2 + (y-y_i)^2} + \sqrt{(x-x_j)^2 + (y-y_j)^2}]/l_{ij}$, with l_{ij} being the distance between the actuator # i and sensor # j . α is a scaling parameter that controls the size of the effective elliptical distribution area of individual sensing paths. The scaling parameter is independent of wave velocity and is empirically determined, which is selected as $\alpha = 1.05$ [24] in this study. A small scaling parameter reduces the size of the affected zone, introducing artifacts, while a large scaling parameter enlarges the size of the affected zone, resulting in the loss of resolution [24,25]. When $B_{ij}(x, y) = 1$, i.e., the point (x, y) is on the direct wave path of the actuator-sensor pair ($\#i, \#j$), $P_{ij}(x, y) = \text{SDC}_{ij}$; when $B_{ij}(x, y) = \alpha$, i.e., the point (x, y) lies on the boundary of the effective distribution area, $P_{ij}(x, y) = 0$. Based on Eq. (4), the location where the debonding is located will have significantly larger probability values compared to the other locations.

In the experiment, nine piezoelectric patches are used for the distributed actuator/sensor network, as shown in Fig. 6. The probabilistic distribution image for the debonding is constructed based on Eq. (4). Figure 12 shows the image of the structure using the sensor signals at $f_c = 175$ kHz for a total of 36 actuator-sensor pairs on SP #1. In the figure, the white dots denote the actuator/sensor location, and the rectangular box represents the actual debonding position and size. The color scale of the image is normalized by its maximum value such that the lighter color represents the higher intensity of the image and the darker color represents the lower intensity. In the image, the higher the probability value is, the higher chance the debonding occurs there. As can be seen, the actual debonded area features significantly higher probability values compared to others; however, artifacts are also observed, which result from multiple wave paths and current sparse sensor network. These artifacts can greatly lower resolution of the debonding image and accuracy of debonding detection.

B. Multifrequency GW Image Fusion

Image fusion refers to the technique of combining or fusing multiple images with the goal of achieving an improved image [30]. To enhance the quality of debonding identification, the image fusion technique is conducted based on the transmitted GWs. Several algorithms can be considered for image fusion, and the most effective fusion process to reduce artifacts is to take the minimum pixel value [30]. Consequently, in the study, the pixel value of the fused image is taken as the minimum value of all the corresponding pixels of the individual images. Figure 13a shows the fused image from 15 images at the frequencies from 150 to 375 kHz based on the proposed algorithm. The color scale of the obtained image is normalized by its maximum value in the figure, where the lighter color is for the higher

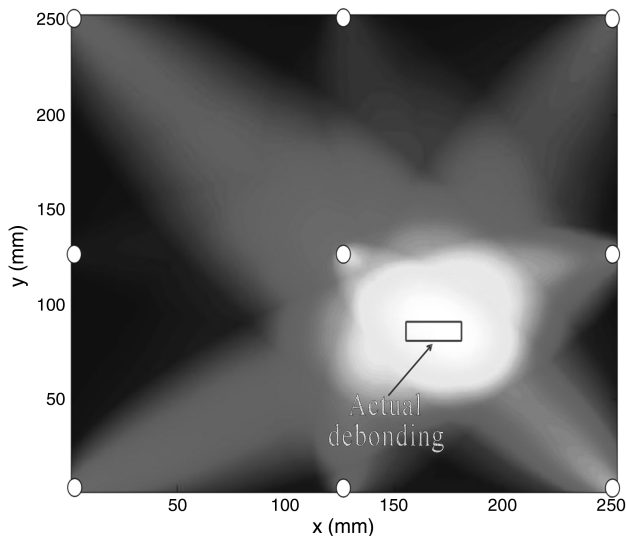
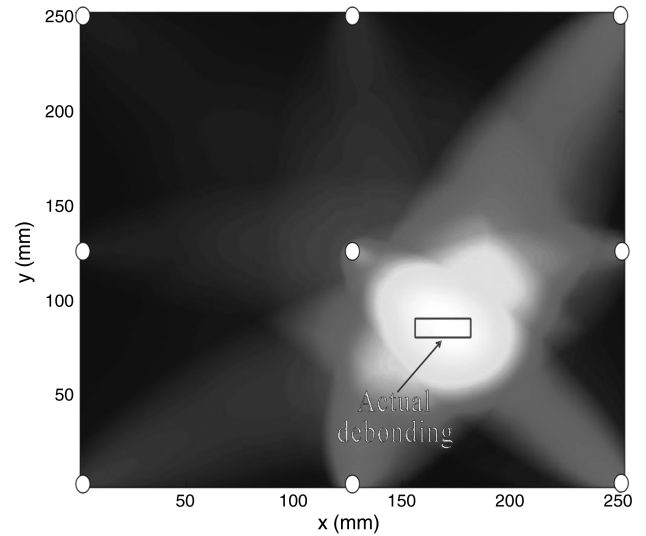
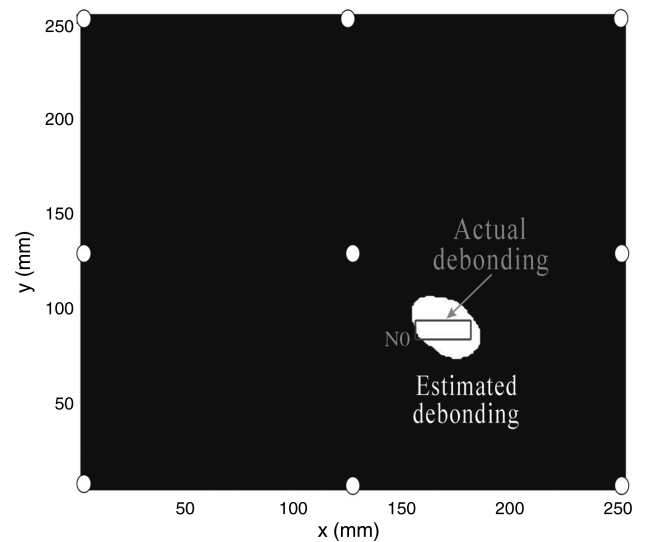


Fig. 12 Debonding image with $f_c = 175$ kHz data for SP #1 (monodebonding).



a)



b)

Fig. 13 a) The fused debonding image using multifrequency GWs on SP #1 (monodebonding), and b) the corresponding binary image by setting up a threshold.

intensity and the darker color is for the lower intensity. Compared with the image in Fig. 12, the quality of the fused image is evidently increased, where fewer artifacts and lower magnitude artifacts indicate better prediction of the debonding. A pixel-intensity-based thresholding is then used to build a binary mask for the constructed damage probability image in Fig. 13a. With a proper threshold value [24] set to the damage probability image, the estimated debonding information is displayed in Fig. 13b. The white area denotes the estimated debonding. It can be observed that the detected debonding agrees with the location of actual debonding. The size of the debonding can also be estimated with satisfactory precision. To evaluate the proposed method, the corresponding debonding locating error is quantitatively listed in Table 3 for the monodebonding N0 on SP#1, which is within a range of a few millimeters. It should be mentioned that different empirical thresholds have been used by different researchers to separate damage from no damage [14,24,31,32]. In the study, the threshold is selected as 90% of the peak intensity of the damage probability image. If the threshold is set to be very low, then virtually everything is classified as damage and the probability of detection approaches 100%, at the expense of false alarms. Conversely, if the threshold is set to be very high, there are no false alarms but at the expense of a dramatically reduced probability of detection [32].

Table 3 Summary of damage detection results in the experimental testing

Case	Actual debonding location, mm	Estimated debonding location, mm	Debonding locating error
SP #1 (N0)	(171.8, 88.6)	(173.6, 91.2)	3.2
SP #2 (N1)	(176.7, 206.3)	(178.6, 209.3)	3.6
SP #2 (N2)	(86.0, 78.5)	(90.1, 83.0)	6.1

C. Multidebonding Detection

Following the similar manner of monodebonding identification, the honeycomb sandwich panel with dual-debonding (SP #2) is evaluated using the same probability analysis approach and multifrequency image fusion. The arrangement of the PZT actuator-sensor network is shown in Fig. 6b. Figure 14 shows the fused image from 15 images at the frequencies from 150 to 375 kHz, where the image is normalized to its maximum value. As evidenced in the figure, both dual-debonding locations can be clearly visualized. However, a pseudodebonding image is also presented, which has almost comparably high damage probability. The existence of the pseudodebonding image is due to the probability coupling between different actuator-sensor pairs.

A detailed illustration of the coupling image paths is given in Fig. 15. In view of current sensor network arrangements and dual-debonding locations, the signals from both actuator-sensor pairs, (#2, #7) and (#4, #9), can contribute to large damage probability values, and the pseudodebonding image is produced at the intersection of these image paths.

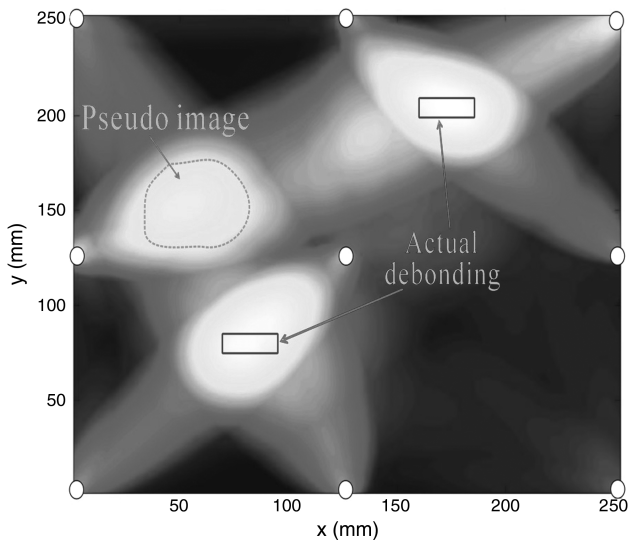


Fig. 14 Fused image with multifrequency GW data for SP #2 (dual-debonding).

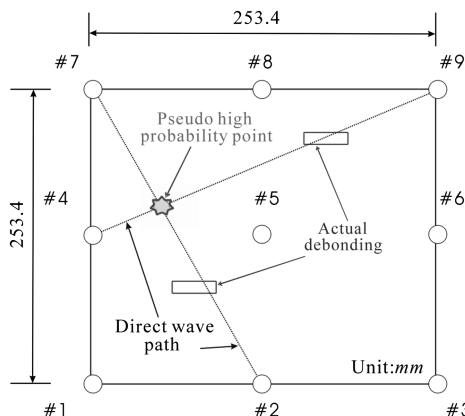


Fig. 15 Illustration of the formation of the pseudodamage image for the evaluation of SP #2 (dual-debonding).

of multifrequency GW image fusion cannot remove the pseudodamage image, because the image pixels on all individual images may have large damage probability intensity within the pseudodebonding image area. Additional effort is needed to rule out the pseudodebonding image.

To eliminate the pseudodamage image, a multilevel sensor network strategy is proposed as shown in Fig. 16. Another 16 auxiliary PZT patches (denoted by a grey dot) are surface-bonded on the larger area of SP#2 to form four sensor subnetworks in a square grid pattern with the same patch-patch distance as the original sensor arrangement (I–IV, see Fig. 16a). The original sensor network within nine PZT actuators/sensors (represented by a white dot) is first used for the center area inspection (colored in light grey) as the first-level evaluation. If multiple damage is found in the first-level testing, the subnetworks (I–IV) will be activated for the second-level evaluation individually. In each individual subnetwork, the similar procedure in Sec. IV.A. for monodebonding detection can apply. Figure 16b shows the images in each subnetwork (I–IV) at $f_c = 200$ KHz by performing the second-level examination. The image is normalized by its maximum value. As demonstrated in the figure, no damage is found in subnetworks I and IV; however, individual monodebonding is clearly visible in subnetworks II and III. The pseudodamage image in subnetwork I can thus be identified by conducting the consistency analysis. By ruling out the pseudoimage and selecting the proper threshold value, the final image of SP #2 bearing dual-debonding can be obtained in Fig. 17. It can be found that the estimated multidebonding information is fairly consistent with the actual occurrence. The corresponding debonding locating error for multidebonding N1 and N2 on SP#2 can be found in Table 3. Compared with the case of monodebonding, the debonding locating error for multidebonding is slightly increased, but the precision can still be considered satisfactory.

Because the design goal of an SHM system is to implement the most structural coverage with the least number of sensors, the optimal sensor spacing needs to be considered for SHM deployments on real structures. To do so, users can specify an acceptable signal loss based on the voltage sensitivity of the data acquisition system, from which the desirable actuator-sensor spacing can be calculated. It should be mentioned that the sensor spacing can also influence the resolution of the damage detection system [33], and therefore comprehensive consideration of the sensor spacing along with the actuating frequency and wavelength of transmitting waves is necessary to optimize these design parameters. More details about selection of optimal SHM system parameters can be found in [34]. Practically, only the hot spots (e.g., fuselage and wings of aircrafts, or other load-bearing structural elements) that are known to be prone to damage will be instrumented with the proposed sparse sensor network due to cost and weight concerns. These mentioned factors should be considered to minimize the system mass/space penalties for aerospace structures.

D. The Framework of Debonding Detection

This subsection summarizes the framework of debonding detection using the sparse piezoelectric actuator/sensor network in honeycomb sandwich structures. Figure 18 shows the flow diagram of the current debonding detection strategy in honeycomb sandwich structures. First, the finite element method is used to understand the wave propagation mechanism in honeycomb sandwich structures, such as wave leaky properties, the wave mode sensitivity to debonding, and debonding effects on wave signals. The understanding from the FE simulation is then used to guide the experimental testing. By appropriately selecting the actuator-sensor

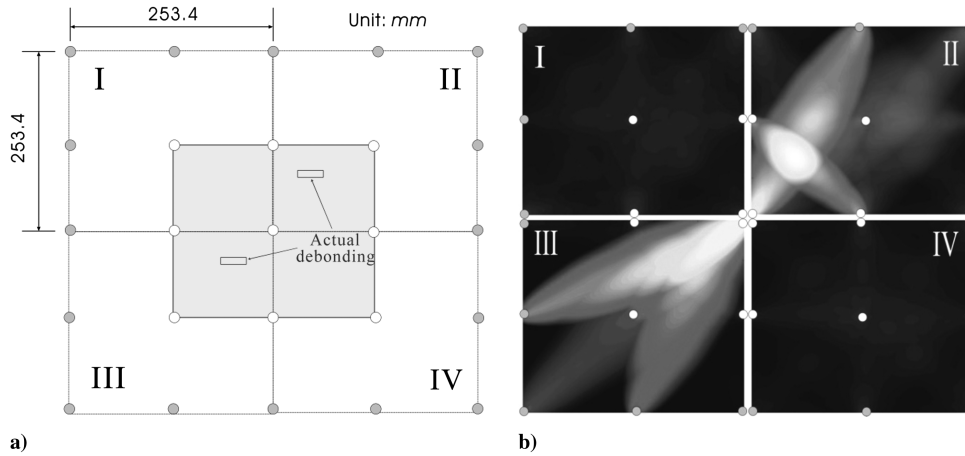


Fig. 16 Multilevel sensor network to identify the pseudodebonding image: a) conceptual view, and b) debonding image in the subnetworks I–IV.

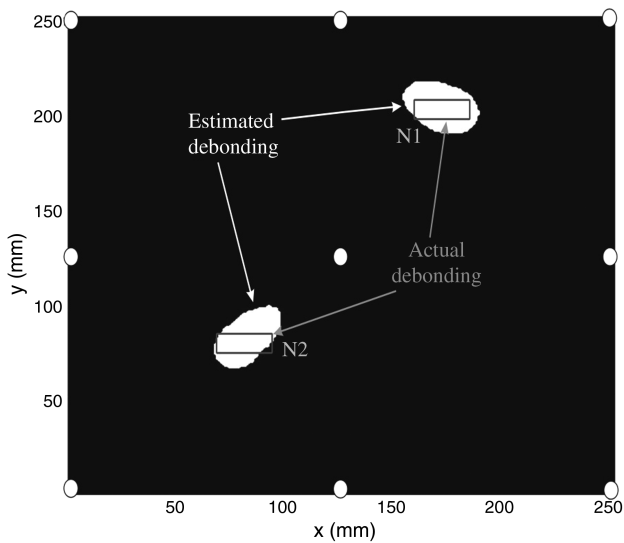


Fig. 17 The corresponding binary image evaluated on SP #2 with dual-debonding by setting zero probability value for pseudodamage area and selecting a proper threshold.

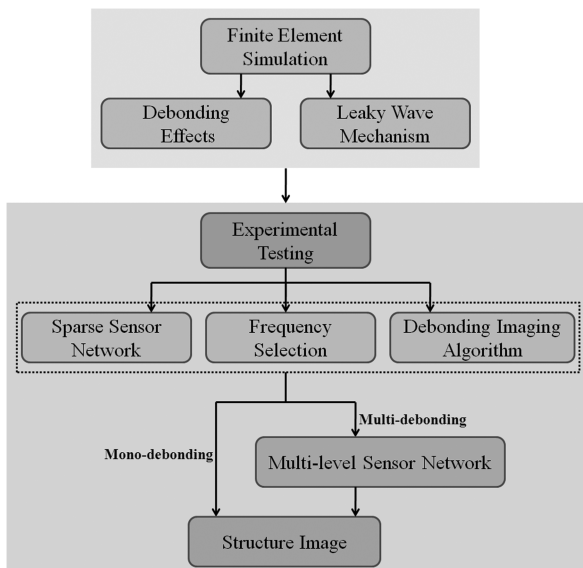


Fig. 18 Flow diagram of debonding detection strategy in honeycomb sandwich structures.

distance and the excitation frequency, a debonding imaging algorithm is proposed based on the differential features of skin-core debonding. The image fusion scheme is performed to increase image quality for both monodebonding and multidebonding cases. For the multidebonding case, a multilevel sensor network is suggested.

V. Conclusions

In this study, effects of skin-core debonding on the leaky guided wave propagation in honeycomb sandwich structures are studied using finite element simulation. In the numerical simulation, a commercially available finite element (FE) code, ANSYS/Multiphysics, is used to simulate wave propagation and wave reception by the surface-bonded piezoelectric actuators/sensors. The coupled electromechanical behavior is considered by directly applying electric voltages. An experimental study is then conducted to verify the numerical simulation and for damage identification. An appropriate signal difference coefficient is defined to represent the differential features of debonding. The measurement noises are filtered out by using a Fourier transform filter method. A damage localization image at each frequency is constructed by conducting probability analysis of differential features of transmitted guided waves in honeycomb sandwich structure with and without debonding for each actuator-sensor pair. An imaging area is then reconstructed by superimposing the image from each actuator-sensor path. The final image of the structure can be subsequently obtained by the approach of image fusion to increase the quality of the image. To detect multiple debondings in the honeycomb sandwich structure, a multilevel sensor network strategy is proposed. The results indicate that the proposed method can provide reliable quantitative information about location and size of debonding in the honeycomb sandwich structure.

Acknowledgments

This research was partly supported by National Natural Science Foundation of China under Grant No. 10832002, the National Science Foundation Grant No. EPS-0701890, and the NASA EPSCoR RID grant. The authors wish to thank both reviewers for their insights and invaluable suggestions, which significantly improved the quality of the work.

References

- [1] Fatemi, J., and Lemmen, M. H. J., "Effective Thermal/Mechanical Properties of Honeycomb Core Panels for Hot Structure Applications," *Journal of Spacecraft and Rockets*, Vol. 46, No. 3, 2009, pp. 514–525. doi:10.2514/1.30408
- [2] Olympio, K. R., and Gandhi, F., "Modeling and Numerical Analyses of Skin Design Concepts," *50th AIAA/ASME/ASCE/AHS/ASC Structures, Structural Dynamics, and Materials Conference*, AIAA, Reston, VA, 2009.
- [3] Davies, G. A. O., Hitchings, D., and Ankersen, J., "Predicting

- Delamination and Debonding in Modern Aerospace Composite Structures,” *Composites Science and Technology*, Vol. 66, No. 6, 2006, pp. 846–854.
doi:10.1016/j.compscitech.2004.12.043
- [4] Wait, J. R., Park, G., Sohn, H., and Farrar, C. R., “An Integrated Active Sensing System for Damage Identification and Prognosis,” *45th AIAA/ASME/ASCE/AHS/ASC Structures, Structural Dynamics, and Materials Conference*, AIAA, Reston, VA, 2004.
- [5] Kosmatka, J. B., and Oliver, J., “Development of an In-Flight Structural Health Monitoring System for Composite Unmanned Aircraft,” *47th AIAA/ASME/ASCE/AHS/ASC Structures, Structural Dynamics, and Materials Conference*, AIAA, Reston, VA, 2006.
- [6] Cuc, A., Giurgiutiu, V., Joshi, S., and Tidwell, Z., “Structural Health Monitoring with Piezoelectric Wafer Active Sensors for Space Applications,” *AIAA Journal*, Vol. 45, No. 12, 2007, pp. 2838–2850.
doi:10.2514/1.26141
- [7] Ihn, J. B., and Chang, F.-K., “Pitch-Catch Active Sensing Methods in Structural Health Monitoring for Aircraft Structures,” *Structural Health Monitoring: An International Journal*, Vol. 7, No. 1, 2008, pp. 5–19.
doi: 10.1177/1475921707081979
- [8] Huang, G. L., Song, F., and Wang, X. D., “Quantitative Modeling of Coupled Piezo-Elastodynamic Behavior of Piezoelectric Actuators Bonded to an Elastic Medium for Structural Health Monitoring: A Review,” *Sensors*, Vol. 10, No. 4, 2010, pp. 3681–3702.
doi:10.3390/s100403681
- [9] Raghavan, A., and Cesnik, C. E. S., “Review of Guided-Wave Structural Health Monitoring,” *The Shock and Vibration Digest*, Vol. 39, No. 2, 2007, pp. 91–114.
doi:10.1177/0583102406075428
- [10] Giurgiutiu, V., Yu, L., Kendall, J. R., III, and Jenkins, C., “In Situ Imaging of Crack Growth with Piezoelectric-Wafer Active Sensors,” *AIAA Journal*, Vol. 45, No. 11, 2007, pp. 2758–2769.
doi:10.2514/1.30798
- [11] Lestari, W., and Qiao, P. Z., “Application of Wave Propagation Analysis for Damage Identification in Composite Laminated Beams,” *Journal of Composite Materials*, Vol. 39, No. 22, 2005, pp. 1967–1984.
doi:10.1177/0021998305052021
- [12] Wu, Z., Qing, X. P., and Chang, F. K., “Damage Detection for Composite Laminate Plates with a Distributed Hybrid PZT/FBG Sensor Network,” *Journal of Intelligent Material Systems and Structures*, Vol. 20, No. 9, 2009, pp. 1069–1077.
doi:10.1177/1045389X08101632
- [13] Purekar, A. S., and Pines, D. J., “Damage Detection in Thin Composite Laminates Using Piezoelectric Phased Sensor Arrays and Guided Lamb Wave Interrogation,” *Journal of Intelligent Material Systems and Structures*, Vol. 21, No. 10, 2010, pp. 995–1010.
doi:10.1177/1045389X10372003
- [14] Su, Z., and Ye, L., “Fundamental Lamb Mode-Based Delamination Detection for CF/EP Composite Laminates Using Distributed Piezoelectrics,” *Structural Health Monitoring: An International Journal*, Vol. 3, No. 1, 2004, pp. 43–68.
doi: 10.1177/1475921704041874
- [15] Su, Z., Li, C., Wang, X. M., Yu, L., and Zhou, C., “Predicting Delamination of Composite Laminates Using an Imaging Approach,” *Smart Materials and Structures*, Vol. 18, No. 7, 2009, 074002.
doi:10.1088/0964-1726/18/7/074002
- [16] Wang, L., and Yuan, F. G., “Damage Identification in a Composite Plate Using Prestack Reverse-Time Migration Technique,” *Structural Health Monitoring: An International Journal*, Vol. 4, No. 3, 2005, pp. 195–211.
doi: 10.1177/1475921705055233
- [17] Petculescu, G., Krishnaswamy, S., and Achenbach, J. D., “Group Delay Measurements Using Modally Selective Lamb Wave Transducers for Detection and Sizing of Delaminations in Composites,” *Smart Materials and Structures*, Vol. 17, No. 1, 2008, 015007.
doi:10.1088/0964-1726/17/01/015007
- [18] Bourasseau, N., Moulin, E., Delebarre, C., and Bonniau, P., “Radome Health Monitoring with Lamb Waves: Experimental Approach,” *Nondestructive Testing and Evaluation*, Vol. 33, No. 6, 2000, pp. 393–400.
doi: 10.1016/S0963-8695(00)00007-4
- [19] Song, F., Huang, G. L., and Hudson, K., “Guided Wave Propagation in Honeycomb Sandwich Structures Using a Piezoelectric Actuator/Sensor System,” *Smart Materials and Structures*, Vol. 18, No. 12, 2009, 125007.
doi:10.1088/0964-1726/18/12/125007
- [20] Hay, T. R., Wei, L., and Rose, J. L., “Rapid Inspection of Composite Skin-Honeycomb Core Structures with Ultrasonic Guided Waves,” *Journal of Composite Materials*, Vol. 37, No. 10, 2003, pp. 929–939.
doi:10.1177/0021998303037010005
- [21] He, F. C., Zhou, Z. G., and Feng, Z. Y., “Research on an Inspection Method for De-bond Defects in Aluminum Skin-Honeycomb Core Sandwich Structure with Guided Waves,” *17th World Conference on Nondestructive Testing*, British Institute of Non-Destructive Testing, Northampton, England, 2008.
- [22] Qi, X., Rose, J. L., and Xu, C. G., “Ultrasonic Guided Wave Nondestructive Testing for Helicopter Rotor Blades,” *17th World Conference on Nondestructive Testing*, British Institute of Non-Destructive Testing, Northampton, England, 2008.
- [23] Baid, H., Banerjee, S., Joshi, S., and Mal, A., “Detection of Disbonds in a Honeycomb Composite Structure Using Guided Waves,” *Proceedings of Health Monitoring of Structural and Biological Systems 2008*, SPIE, Bellingham, WA, 2008.
- [24] Zhao, X. L., Gao, H. D., Zhang, G. F., Ayhan, B., Yan, F., Kwan, C., and Rose, J. L., “Active Health Monitoring of an Aircraft Wing with Embedded Piezoelectric Sensor/Actuator Network: 1. Defect Detection, Localization and Growth Monitoring,” *Smart Materials and Structures*, Vol. 16, No. 4, 2007, pp. 1208–1217.
doi:10.1088/0964-1726/16/4/032
- [25] Wang, D., Ye, L., Lu, Y., and Li, F., “A Damage Diagnostic Imaging Algorithm Based on the Quantitative Comparison of Lamb Wave Signals,” *Smart Materials and Structures*, Vol. 19, No. 6, 2010, 065008.
doi:10.1088/0964-1726/19/6/065008
- [26] Lin, X., and Yuan, F. G., “Detection of Multiple Damages by Prestack Reverse-Time Migration,” *AIAA Journal*, Vol. 39, No. 11, 2001, pp. 2206–2215.
doi:10.2514/2.1220
- [27] Su, Z., Wang, X. M., Chen, Z. P., and Ye, L., “A Hierarchical Data Fusion Scheme for Identifying Multi-Damage in Composite Structures with a Built-in Sensor Network,” *Smart Materials and Structures*, Vol. 16, No. 6, 2007, pp. 2067–2079.
doi:10.1088/0964-1726/16/6/010
- [28] Dutta, D., “Ultrasonic Techniques for Baseline-Free Damage Detections in Structures,” Ph.D. Dissertation, Civil and Environmental Dept., Carnegie Mellon University, Pittsburgh, PA, 2010.
- [29] Yan, F., Royer, R. L., Jr., and Rose, J. L., “Ultrasonic Guided Wave Imaging Techniques in Structural Health Monitoring,” *Journal of Intelligent Material Systems and Structures*, Vol. 21, No. 3, 2010, pp. 377–384.
doi:10.1177/1045389X09356026
- [30] Michaels, J. E., and Michaels, T. E., “Guided Wave Signal Processing and Image Fusion for In Situ Damage Localization in Plates,” *Wave Motion*, Vol. 44, No. 6, 2007, pp. 482–492.
doi:10.1016/j.wavemoti.2007.02.008
- [31] Ng, C. T., and Veidt, M., “A Lamb-Wave-Based Technique for Damage Detection in Composite Laminates,” *Smart Materials and Structures*, Vol. 18, No. 7, 2009, 074006.
doi: 10.1088/0964-1726/18/7/074006
- [32] Michaels, J. E., “Ultrasonic Structural Health Monitoring: Strategies, Issues and Progress,” *Proceedings of Smart Sensor Phenomena, Technology, Networks, and Systems*, SPIE, Bellingham, WA, 2008.
- [33] Sohn, H., Park, G., Wait, G. R., Limback, N. P., and Farrar, C. R., “Wavelet-Based Active Sensing for Delamination Detection in Composite Structures,” *Smart Materials and Structures*, Vol. 13, No. 1, 2004, pp. 153–160.
doi:10.1088/0964-1726/13/1/017
- [34] Kessler, S. S., “Piezoelectric-Based In-Situ Damage Detection of Composite Materials for Structural Health Monitoring Systems,” Ph.D. Dissertation, Aeronautics and Astronautics Dept., Massachusetts Institute of Technology, Cambridge, MA, 2002.